

Non-destructive imaging of residual strains in GaN and their effect on optical and electrical properties using correlative light-electron microscopy

Cite as: J. Appl. Phys. **131**, 075303 (2022); <https://doi.org/10.1063/5.0080024>

Submitted: 27 November 2021 • Accepted: 26 January 2022 • Published Online: 16 February 2022

 G. Naresh-Kumar,  P. R. Edwards,  T. Batten, et al.



View Online



Export Citation



CrossMark

ARTICLES YOU MAY BE INTERESTED IN

Realizing crack-free high-aluminum-mole-fraction AlGaIn on patterned GaN beyond the critical layer thickness

Journal of Applied Physics **131**, 073103 (2022); <https://doi.org/10.1063/5.0073489>

Optical anisotropy of (11 $\bar{2}$ 3) semipolar InGaIn quantum wells homoepitaxially grown on GaN substrates

Journal of Applied Physics **131**, 074502 (2022); <https://doi.org/10.1063/5.0081815>

Nanoscale imaging of dopant incorporation in n-type and p-type GaN nanowires by scanning spreading resistance microscopy

Journal of Applied Physics **131**, 075701 (2022); <https://doi.org/10.1063/5.0080713>

Lock-in Amplifiers up to 600 MHz



Zurich
Instruments



Non-destructive imaging of residual strains in GaN and their effect on optical and electrical properties using correlative light-electron microscopy

Cite as: J. Appl. Phys. 131, 075303 (2022); doi: 10.1063/5.0080024

Submitted: 27 November 2021 · Accepted: 26 January 2022 ·

Published Online: 16 February 2022



G. Naresh-Kumar,^{1,a)} P. R. Edwards,¹ T. Batten,² M. Nouf-Alleghiani,¹ A. Vilalta-Clemente,³ A. J. Wilkinson,³ E. Le Boulbar,⁴ P. A. Shields,⁴ B. Starosta,¹ B. Hourahine,¹ R. W. Martin,¹ and C. Trager-Cowan¹

AFFILIATIONS

¹Department of Physics, SUPA, University of Strathclyde, Glasgow G4 0NG, United Kingdom

²Renishaw plc, Wotton-under-Edge, Gloucestershire GL12 8JR, United Kingdom

³Department of Materials, University of Oxford, Parks Road, Oxford OX1 3PH, United Kingdom

⁴Department of Electronic and Electrical Engineering, University of Bath, Bath BA2 7AY, United Kingdom

^{a)}Author to whom correspondence should be addressed: naresh.gunasekar@strath.ac.uk

ABSTRACT

We demonstrate a non-destructive approach to understanding the growth modes of a GaN thin film and simultaneously quantify its residual strains and their effect on optical and electrical properties using correlative scanning electron microscopy techniques and Raman microscopy. Coincident strain maps derived from electron backscatter diffraction, cathodoluminescence, and confocal Raman techniques reveal strain variations with similar magnitude and directions, especially in the proximity of dislocations. Correlating confocal Raman imaging with electron channeling contrast imaging suggests that the dislocations organize themselves to form a distinctive pattern as a result of the underlying growth mask, where some of them align along the [0001] growth direction and some are inclined. The methodology presented in this work can be adopted to investigate any heteroepitaxial growth, in particular, those using selective masks on the growth substrates, where the morphology influences the subsequent growth.

© 2022 Author(s). All article content, except where otherwise noted, is licensed under a Creative Commons Attribution (CC BY) license (<http://creativecommons.org/licenses/by/4.0/>). <https://doi.org/10.1063/5.0080024>

I. INTRODUCTION

Measuring strain relaxation in lattice-mismatched heteroepitaxial semiconductor materials, for example, GaN, provides insight into dislocation formation.¹ Understanding the nature of dislocations and their role in plastic deformation helps us to better develop novel methods for producing technologically relevant electronic materials. Extended defects in as-grown semiconductors are quite common, especially in the heteroepitaxial growth of thin films, irrespective of the growth methods and conditions. Screw dislocations, for example, can alter the activation barrier for growth in the immediate surrounding areas^{2,3} and can be detrimental to electronic and optoelectronic devices.^{4,5} There are papers on the growth and structural characterization of a wide range of semiconductors, where the strain state and dislocations of the grown material were quantified, often using destructive

and indirect analytical techniques.^{1,6} There is also extensive literature on non-destructive imaging of extended defects and residual strain evaluation methods.^{6–8} However, we know of no reports describing the non-destructive evaluation of the residual strains and the correlation of these with the arrangement of dislocations, and their effect on optical and electrical properties from the same microscale region of the sample. This is the objective of our work.

Here, we demonstrate a non-destructive approach to understanding semiconductor thin film growth modes, studying the structural, optical, and electrical properties of a thin film using correlative light-electron microscopy. We combine the scanning electron microscope (SEM) based techniques of high spatial resolution electron backscattered diffraction (EBSD),⁷ electron channeling contrast imaging (ECCI),⁸ and cathodoluminescence (CL) hyperspectral

imaging⁹ together with confocal Raman hyperspectral imaging¹⁰ to image and quantify the residual strains in a nanodash epitaxial lateral overgrown (ELOG) GaN thin film. We have chosen GaN due to its technological importance,¹¹ and as an example to demonstrate our correlative microscopy approach. Nonetheless, our methodology is suitable for any heteroepitaxial thin film growth, especially when using selective masks on the growth substrate.

II. EXPERIMENTAL METHODS

Confocal Raman imaging is performed using a Renishaw inVia confocal Raman microscope with a 532 nm laser source, 3000 lines/mm grating, and 150 \times (0.95 NA) objective. The laser power was 10 mW, the lateral spatial resolution was 0.3 μ m, and the spectral shift resolution is better than 0.01 cm^{-1} . Raman maps were obtained by scanning the sample under the microscope using a 0.1 μ m step size. An FEI Sirion 200 Schottky FEG-SEM was used to obtain secondary electron images and ECCI micrographs at an electron beam energy of 30 keV. The ECCI micrographs were obtained using the forescatter geometry where the sample is tilted from 30° to 80° toward the electron-sensitive detector positioned to collect electrons scattered to low takeoff angles. The EBSD patterns were obtained using a Bruker e⁺Flash^{HR+} EBSD detector mounted on a Merlin (Zeiss) FE-SEM with an electron beam energy of 20 keV and a probe current of \approx 5 nA. By moving a focused electron beam point by point across a grid of positions on the surface of the sample, the EBSD maps were recorded by acquiring an EBSD pattern for every 150 nm with a pattern resolution of 1600 \times 1200 pixels (full resolution of the EBSD camera) and exposure time of 1 s per pattern. The residual strain and lattice rotation maps were calculated using cross-correlational analysis conducted offline using the method described in Refs. 12 and 13. EBSD pattern shifts were determined from 35 ROIs of each pattern with a bandpass filter applied in the Fourier domain to remove high-frequency noise and low-frequency background intensity variations. One pattern was selected as the reference and all the measurements are made relative to this. An FEI Quanta 250 Schottky FEG-SEM was used to perform CL in hyperspectral imaging mode using a custom-built CL system attached to the SEM, where a spectrally resolved luminescence spectrum is collected for every pixel in the image. The light was collected by a Schwarzschild reflecting objective, dispersed with a 1/8 m focal length spectrometer (Oriel MS125), and collected using a 1600-channel electron-multiplying charge-coupled device (Andor Newton). The CL data set was recorded at room temperature with an electron beam energy of 5 keV.

A. Growth of nanodash GaN

The nanodash ELOG growth of GaN is described in detail in Ref. 14. Here, we briefly describe the nanodash fabrication and subsequent growth. Typically, in the selective area growth of GaN, a dielectric material (SiN_x in our case) is used to produce a pattern on top of a GaN layer; further material cannot nucleate where the dielectric material is present. Electron beam lithography combined with dry etching is used to create openings in the form of dashes with nanoscale dimensions. Further growth from the nanodashes is described below. The growth procedure can be divided into three

stages described by these terms: (a) convex, (b) concave, and (c) planarization. The nanodashes aligned along $\langle 1-100 \rangle$ are used to promote lateral growth during the convex growth phase. After the first 20 min of growth, a highly regular pattern of elongated pyramid dashes is created as shown in the secondary electron (SE) image in Fig. 1(a). Each dash is made up of six slow-growing $\{1-101\}$ facets and two fast-growing $\{11-22\}$ facets, the latter laterally enlarging the nanostructures to create more diamond-like shapes with further growth. Each nanodash meets its neighbors after around 200 min growth, at which stage the $\{11-22\}$ facet from one structure touches the $\{1-101\}$ facet of an adjacent one, as seen in Fig. 1(b). At this point, the growth switches from convex to concave, after which the growth rate increases and the structure evolves into a highly regular tessellation of $\{1-101\}$ and $\{0001\}$ *c*-plane facets. Further continuing the growth, at around 560 min, the selective growth mask is completely covered to create an array of large inverted pyramids, each bounded by two coexisting families of semipolar planes: $\{1-101\}$ and $\{11-22\}$ [see Fig. 1(c)]. Planarization using a higher growth temperature was initiated once the growth mask was completely covered to result in nominally undoped *c*-plane GaN at around 880 min with slight undulations in the surface [see Fig. 1(d)].

III. RESULTS AND DISCUSSION

A. Confocal Raman imaging and SEM imaging

Although the SE images shown in Figs. 1(a)–1(d) clearly depict various stages of the crystal growth, one has to stop the growth and capture the image to understand the evolution of the crystal growth using this method. Here, we propose an alternative approach to understanding the growth mechanism without interrupting the crystal growth, while simultaneously probing some of the physical properties of the grown material both rapidly and non-destructively by using confocal Raman imaging. In the past, Raman measurements¹⁵ have been slow, with a single spectrum typically taking up to a minute to acquire. However, advances in technology have significantly reduced this time to milliseconds,¹⁶ enabling large area mapping measurements in 3D with sub-micrometer spatial resolution.¹⁷ Figures 1(e)–1(h) show confocal Raman E_2 peak¹⁵ intensity images taken at different depths through a sample.¹⁸ Although the confocal Raman images do not have as high a lateral spatial resolution as the SE images, the nanodash structures and their evolution at the various stages of growth can clearly be observed. The information from the overlying layers is largely excluded in the confocal image acquired from the deeper part of the sample. The [supplementary material](#) (S1) contains a video of confocal Raman imaging showing the evolution from nanodashes to a completely coalesced thin film.

The possibility of using multiple analysis modes has been one of the major advantages of using an SEM along with minimal or no sample preparation and the ability to study bulk as well as nanoscale structures (from a few millimeters to nanometers). Detailed descriptions of different analysis modes, techniques, and their uses are given elsewhere.^{19,20} Here, we describe how we exploit some of the SEM-based techniques to understand the strain state and distribution of dislocations,^{12,21,22} thereby revealing the growth mechanisms which result from the underlying nanodash

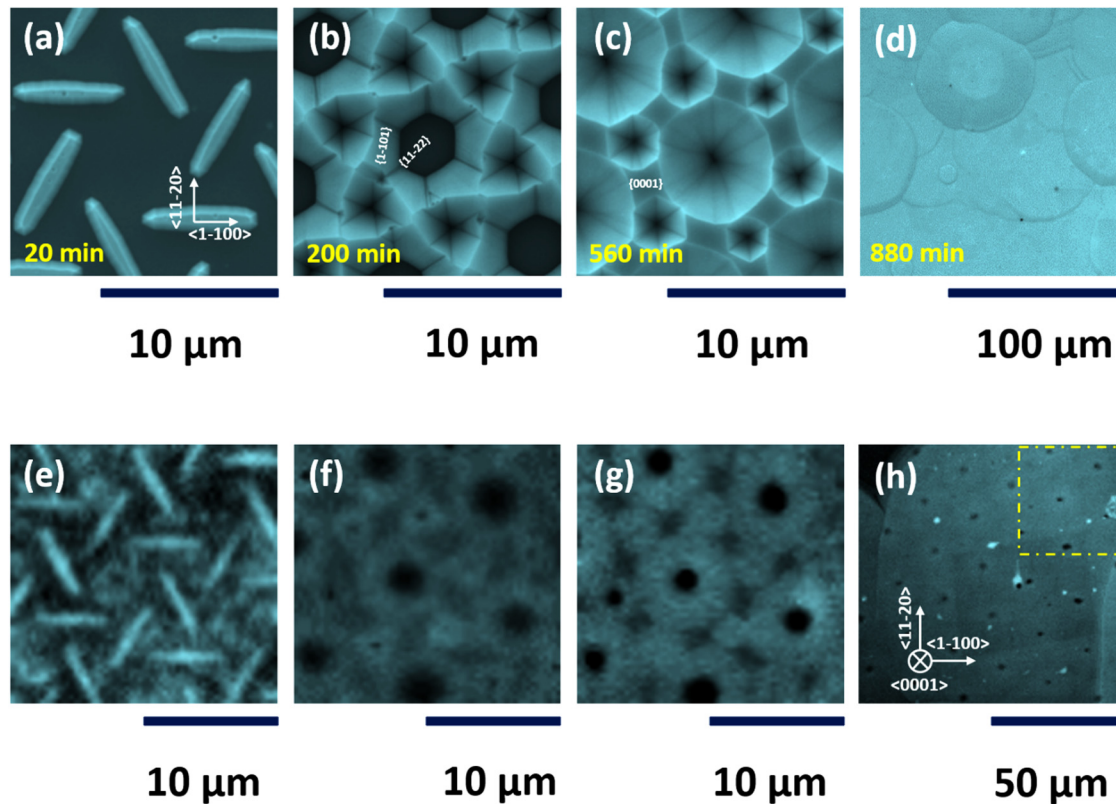


FIG. 1. Evolution of crystal growth morphology monitored during the various stages of the nanodash GaN thin film structure imaged using secondary electrons (SEs) in a scanning electron microscope [(a)–(d)] and confocal Raman images [(e)–(h)] of E_2 peak intensity. The SE images were taken after interrupting the growth to record the growth modes and not from the same sampling area, whereas the confocal images were taken after the growth and from the same micrometer-scale area of the sample. (e)–(g) were collected at 18.3, 9.2, and 4.6 μm beneath the sample surface; their exact location is highlighted on the larger sample area image in (h).

template. We have performed ECCI followed by EBSD, CL, and Raman imaging. Figure 2 shows coincident white light microscopy, confocal Raman microscopy, and scanning electron microscopy images from the same micrometer-scale area of the nanodash GaN

thin film. The images are cropped to display the same area to directly compare the various properties of the sample. Optical microscopy is useful for acquiring large areas with prominent features that can be used as reference markers for finding the same

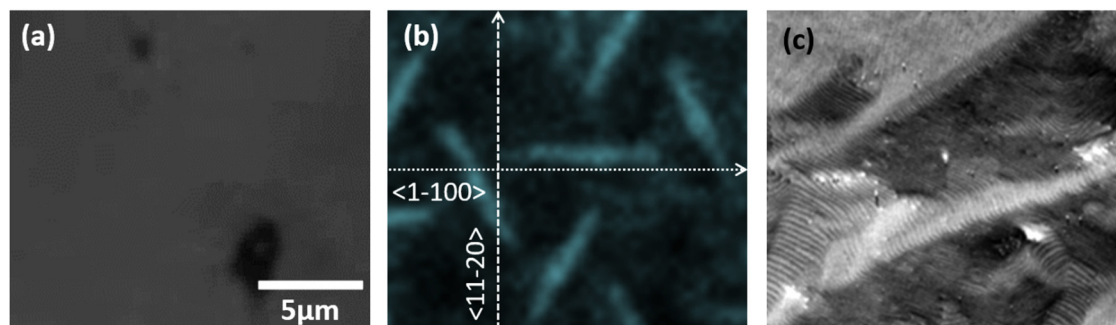


FIG. 2. Coincident optical, confocal Raman, and scanning electron microscopy imaging. (a) The white light optical image, (b) confocal Raman image of E_2 peak intensity collected 16 μm beneath the sample surface, and (c) topographic contrast dominated backscatter electron image.

area for other characterization techniques. Since GaN is transparent in the visible region of the spectrum, we sought out areas close to contamination spots to help registration; this is shown in Fig. 2(a). Nonetheless, large area optical images (see S2 in the [supplementary material](#)) show areas with surface undulations, which served as recognizable features for aligning our correlative microscopy analysis. The confocal image in Fig. 2(b) is acquired in such a way that the sample is oriented to a specific crystallographic direction as marked in the image. This makes it possible to identify $\langle 1-100 \rangle$ and $\langle 11-20 \rangle$ directions from underlying nanodashes as shown in Fig. 2(b). The surface morphology of the sample is shown clearly in the backscatter electron (BSE) image displayed in Fig. 2(c). Depending on the detector position, direction and energy of the incident, as well as the scattered electrons, BSEs can reveal both topographic and diffraction information.²³ Figure 2(c) shows a topographic-dominated BSE image. In comparison with the E_2 peak intensity Raman image, there is no clear correlation between the surface topography and the nanodash orientation. Nonetheless, there is a correlation between the orientation of nanodashes and the dislocation distribution. Figure 3(a) shows an ECCI micrograph acquired under the channeling

conditions optimized to reveal threading dislocations (TDs), and they appear as spots with bright and dark contrast.

Although it is possible to identify dislocations by ECCI using the invisibility criteria used in transmission electron microscopy (TEM), it is not possible to satisfy the appropriate conditions in a plan view image for vertical TDs in materials where surface relaxation is dominant. Instead, for materials with a wurtzite crystal structure such as GaN, a simple geometric procedure may be used to identify a given TD as an edge (a type), screw (c type), or mixed ($a + c$ type), by exploiting differences in the direction of the dark-bright contrast observed for dislocations in two ECCI micrographs acquired with symmetric channeling conditions.²⁴ As a result of their screw component, dislocations inclined to the surface will be identified as mixed-type dislocations. Under appropriate diffraction conditions, if TDs are inclined to the surface, they may also exhibit lower contrast than vertical TDs. This is observed in the ECCI micrograph in Fig. 3(a) (also see S3 in the [supplementary material](#)). The total TD density is $(6.0 \pm 0.5) \times 10^7 \text{ cm}^{-2}$. The relative percentages of edge, mixed and inclined dislocations vary over the sample, and for the ECCI micrograph in Fig. 3(a), the percentages of dislocations of each

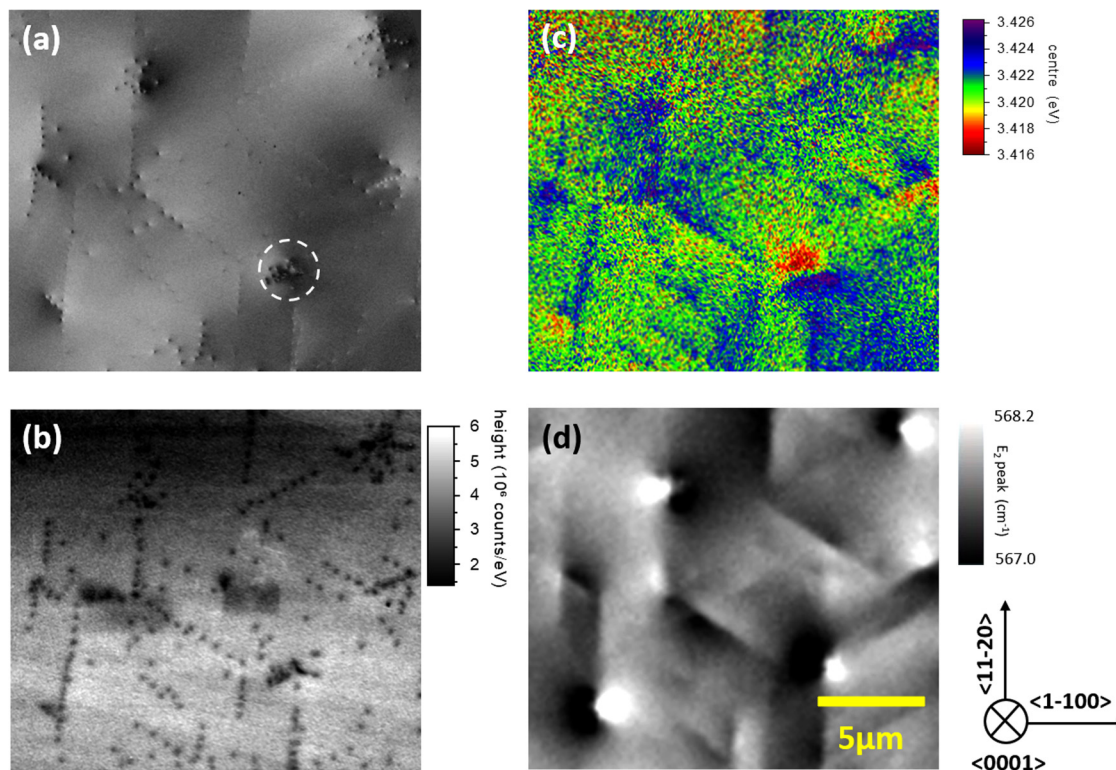


FIG. 3. Coincident ECCI, CL, and confocal Raman imaging. (a) ECCI micrographs show threading dislocations (TDs) as black and white spots. (b) CL NBE intensity map showing TDs as black spots, (c) CL fitted peak position energy map showing compressive (blue region) and tensile strain (red region) on clusters of TDs, and (d) Raman image of the E_2 peak position showing the strain effect due to TDs similar to a CL centroid energy map measurement collected $\approx 2 \mu\text{m}$ beneath the sample surface. The dotted circle shows a region of clustered dislocations.

type were estimated as $\approx 10\%$ edge, $\approx 60\%$ mixed, and $\approx 30\%$ inclined (see S3 in the [supplementary material](#)).

B. Impact of dislocations on optical and electrical properties

Having identified dislocation distribution and types, we now show their impact on the optical and electrical properties with the correlative microscopic techniques of hyperspectral CL and confocal Raman imaging. Wavelength shifts in CL peaks observed in GaN (as for other materials) can be due to the effects of strain, temperature, electron beam energy (depth), carrier concentration, and excitation density.²⁵ Within a single CL hyperspectral image acquired with fixed experimental conditions, only the intrinsic properties of the sample itself, such as strain and carrier concentration, will vary. In our present work, we can rule out the contribution of Si out-diffusion from the ELOG mask as the overgrown thickness of the film is $20\text{ }\mu\text{m}$, leaving strain as the major contributing factor in our analysis. Most of the work on estimating strain from the luminescence peak positions has been carried out at low temperatures on GaN thin films where multiple free excitons (A, B, and C) are observed.²⁶ Since we have performed CL at room temperature, only a single broad peak is observed which we refer to as the near band edge (NBE) emission peak. The NBE peak at room temperature is dominated by the A free exciton, so it is reasonable to assume that the NBE peak has the characteristics and behavior of the A free exciton (see S4 in the [supplementary material](#) for a mean CL spectrum).

For the CL intensity map shown in [Fig. 3\(b\)](#), dark spots corresponding to single, isolated TDs have a diameter of $\approx 150\text{ nm}$. If the excitation volume is sufficiently small, the size of the dark spots is determined by the minority carrier diffusion length. In this case, the size of the dark spots is dominated by the excitation volume.²² The larger dark spots correspond to clusters of TDs. A comparison of the ECCI micrograph and the CL intensity map shows a one-to-one correlation for these TDs. The regions of the sample showing the highest CL intensity appear to coincide with regions of the sample which are free of dislocations. However, not all dislocation-free regions show bright CL, possibly indicating the presence of other defects such as point defects. [Figure 3\(c\)](#) shows the CL fitted peak position energy map where the effect of dislocations on the strain and the effect of strain on the bandgap are mapped. The dislocation clusters show a strain profile from compressive to tensile through a shift in peak emission energy (lower energy for tensile strain and higher energy for the compressive strain). The origin of the shift in the CL NBE peak is due to local strain caused by dislocations. The average energy and full width half maximum (FWHM) of the NBE peak at the defect-free region are 3.421 eV and 55 meV , respectively (see [Fig. S4](#) in the [supplementary material](#)). The average energy of the NBE peak at the center of a dislocation cluster (compressive side) is 3.425 eV . As a first approximation, the magnitude of the energy shift caused by dislocations [19 of them, marked by the dotted white circle in [Fig. 3\(a\)](#)] is $\approx 4\text{ meV}$. Typically, an increase in FWHM corresponds to an increase in the density of dislocations or impurity incorporation. We do not see any appreciable change in the FWHM on our sample (see [Fig. S4](#) in the [supplementary material](#)).

Dislocation strain fields in GaN, probed by confocal Raman imaging, are shown in [Fig. 3\(d\)](#). One of the distinct peaks observed in the Raman spectrum of GaN is the E_2 peak. The position of the E_2 peak of relaxed GaN at room temperature is at 567.6 cm^{-1} .²⁷ Tensile strain in the crystal leads to a shift to a lower frequency and compressive strain leads to a shift to a higher frequency. This is shown in [Fig. 3\(d\)](#) where areas with groups of dislocations show regions of relatively more compressive or tensile strain. The direction of the strain profile (black-white direction) is different for different clustering of dislocations. This is due to the different types of dislocations in the cluster and their inclination angles to the surface. Our Raman measurements indicate that the GaN layer is under average compressive stress of 0.162 GPa . The relative shift of the E_2 peak between the areas with and without dislocations is $\approx 0.6\text{ cm}^{-1}$. Compared with ECCI micrographs, we have related the TD density to the FWHM of the E_2 (high) peak. Regions with no dislocations show lower FWHM and regions with TDs show relatively high FWHM (see S5 in the [supplementary material](#)). This is consistent with the expectation that the smaller the FWHM, the lower the number of extended and point defects.²⁷

C. Imaging residual strains by EBSD, CL, and Raman imaging

Typically, c-plane oriented GaN grown on sapphire by MOCVD exhibits biaxial strain.²⁸ However, in our case due to the complex growth method involving nanodashes, the strain state can be complicated. To further investigate the effect of nanodashes on the residual strain of the GaN thin film, normal and shear strains were calculated from high-resolution (HR) EBSD.^{13,29,30} The results were then compared to the residual strain calculated from CL and Raman imaging. The large area elastic strain variation and lattice rotation maps obtained using the cross-correlational EBSD analysis¹³ are given in S6 and S7 in the [supplementary material](#). Here, we show normal strain distributions obtained using the light and electron microscopy techniques from the same area of a sample. A detailed description of strain measurements by EBSD is given in Refs. 13, 29, and 30 and briefly explained in the [supplementary material](#). Here, we discuss the assumptions made to produce the strain maps. The maps produced represent the variation in elastic strain with respect to a reference point. The reference point is a user-selected option; in our measurements, we have selected an area toward the top left corner of the map where there are no extended defects. A number of square regions of interest (ROIs) are distributed over the electron backscatter diffraction patterns. For each ROI, the cross correlation between the test pattern and the reference pattern is calculated using fast Fourier transforms. The location of the peak in the cross correlation is determined and gives the shift vector for this ROI. The shift measured is the average of all pixels within the ROI. We assume that the shift measured in this way is equal to the shift at the point at the center of the ROI. Similarly, we assume that the measured shifts are some average value determined by the strain within the sample volume in the specimen.

[Figures 4\(a\)](#) and [4\(b\)](#) show the residual normal strain maps; we have added the in-plane strains ($\epsilon_{xx} + \epsilon_{yy}$) and plotted the out-of-plane ϵ_{zz} separately. The same color scale (blue—minimum to red—maximum) is used for plotting residual strains using all

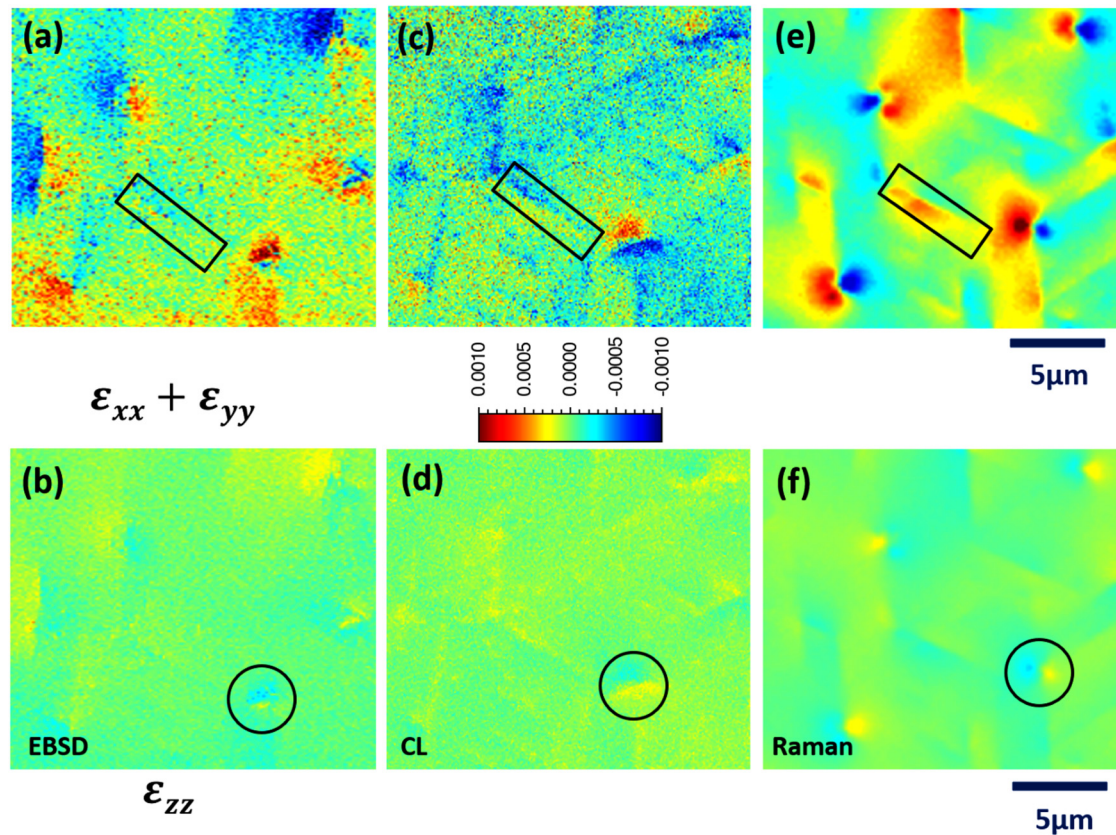


FIG. 4. Residual normal strains distribution derived from high spatial resolution EBSD, CL, and confocal Raman imaging. Top row images correspond to residual strains along $\langle 11\bar{2}0 \rangle$ and $\langle 1\bar{1}00 \rangle$ and bottom row images correspond to residual strain along $\langle 0001 \rangle$. (a) In-plane strain maps from EBSD, (b) out-of-plane strain, along $\langle 0001 \rangle$. Normal strains are derived from CL (c) in-plane strains and (d) out-of-plane strains. Normal strains derived from Raman E_2 peak position map (e) in-plane strains and (f) out-of-plane strain.

three techniques. Regions with high tensile strain are in red, and regions with compressive strain are in blue. Areas with lower strain or no strain are in green. By comparing maps of the six (three normal and three shears) strain components (ϵ_{xx} , ϵ_{yy} , ϵ_{zz} , ϵ_{xy} , ϵ_{xz} , ϵ_{yz}), it can be determined that the higher strain variations are for the in-plane shear strain, ϵ_{xy} , and the two in-plane normal strains, ϵ_{xx} and ϵ_{yy} (see Fig. S6 in the [supplementary material](#)). The lattice constants and in-plane thermal expansion coefficient of the GaN differ from that of sapphire, and this results in the in-plane strain of GaN on sapphire, which will also lead to the formation of dislocations. Regions with dislocations show both high compressive and high tensile strain. The dipole-like strain profile (see S6 in the [supplementary material](#)) is a classic indicator of residual shear strain due to dislocations. The variation in the out-of-plane normal strain (ϵ_{zz}) is minimal (but not completely nil) in accordance with the assumption that the corresponding out-of-plane stresses should be zero.²⁹ From the strain calculations, ϵ_{xx} is not exactly equal to ϵ_{yy} , the condition for true biaxial strain. A cross-correlational plot between ϵ_{xx} and ϵ_{yy} provides a Pearson correlation

coefficient of 0.5, which is significant, and shows that the strain may be anisotropic. The magnitude of the shear strain (ϵ_{xy}) in the areas where there are dislocations is ± 0.0008 . Larger variation in the misorientation is also seen in the regions with more dislocations. The magnitude of the out-of-plane rotations (ω_{xz} and ω_{yz}) are greater than the in-plane rotation (ω_{xy}), indicating a higher density of screw component dislocations compared to edge component dislocations; this is consistent with the ECCI dislocation analysis. Individual dislocations are also resolvable in the ω_{xy} , ω_{xz} , and ω_{yz} EBSD maps (see S7 in the [supplementary material](#)).

We then compare the normal strain evaluated by CL and confocal Raman imaging from the same area as the EBSD and quantify the residual strain. The depth resolution of scanning electron microscopy based techniques such as EBSD and CL can range from tens of nm to hundreds of nm. The depth resolution of the confocal Raman imaging is in the order of hundreds of nm to tens of μm . Note that the EBSD and CL maps have been rescaled since they were acquired at a different tilt angle than the large area Raman image, which is used as a reference for the image alignment.

Shan *et al.*²⁶ investigated the effect of strain on the excitonic transitions of GaN where they measured the strain using x-ray diffraction and the excitonic peak positions using photoluminescence spectroscopy. We have taken a similar approach but we used EBSD for strain measurements and hyperspectral CL imaging for the A free exciton peak position. The A free exciton peak position is related to the principal strains (ϵ_{xx} , ϵ_{yy} , ϵ_{zz}). The relation between the CL peak position and the principal strains can be described by (neglecting spin-orbit interaction)

$$E(A) = E(0) + a_1\epsilon_{zz} + a_2(\epsilon_{xx} + \epsilon_{yy}) + b_1\epsilon_{zz} + b_2(\epsilon_{xx} + \epsilon_{yy}),$$

where $E(0)$ is the strain-free transition energy of the A free exciton peak and $E(A)$ is the energy of the NBE peak position from the hyperspectral CL map. Assuming the out-of-plane stress to be zero, we deduce $\epsilon_{xx} + \epsilon_{yy} = -\frac{C_{33}}{C_{13}}\epsilon_{zz}$, where C_{13} and C_{33} are the stiffness coefficients. We have used the same elastic stiffness coefficients $C_{13} = 106$ GPa and $C_{33} = 398$ GPa, used in our EBSD analysis. This reduces the equation relating to excitonic peak position and strain $\Delta E = (a_1 + b_1)\epsilon_{zz} + (a_2 + b_2)(\epsilon_{xx} + \epsilon_{yy})$. We then resolve $\epsilon_{xx} + \epsilon_{yy}$ and ϵ_{zz} , using the following equations and the strain maps are shown in Figs. 4(c) and 4(d), respectively,

$\epsilon_{xx} + \epsilon_{yy} = \frac{\Delta E}{(a_2 + b_2) - \frac{C_{13}}{C_{33}}(a_1 + b_1)}$ and $\epsilon_{zz} = (\epsilon_{xx} + \epsilon_{yy})\left(-\frac{C_{13}}{C_{33}}\right)$. The constants a_1 and a_2 are the hydrostatic deformation potentials; b_1 and b_2 are the uniaxial deformation potentials. We used the deformation potentials from Wilkinson *et al.*,²⁹ $a_1 = -6.5$ eV, $a_2 = -11.8$ eV, $b_1 = -5.3$ eV, and $b_2 = 2.7$ eV. We then estimated the residual strain from the Raman E_2 peak positions and resolved the normal strains $\epsilon_{xx} + \epsilon_{yy}$ and ϵ_{zz} without including the effect of shear strain,²⁸

$$\Delta\omega = a_{E2}(\epsilon_{xx} + \epsilon_{yy}) + b_{E2}\epsilon_{zz} \pm c_{E2}\sqrt{(\epsilon_{xx} - \epsilon_{yy})^2 + 4\epsilon_{xy}^2},$$

where a , b , and c are the deformation potentials of the E_2 (high) peak with values of -850 , -963 , and 379 cm^{-1} , respectively.²⁸ The magnitude of the residual strain maps derived using all three techniques yield similar values. The residual strain due to dislocations from two regions (i) from clusters of dislocations (see the solid circles in Fig. 4) and (ii) from a line of edge dislocations (see the solid rectangle in Fig. 4) are also estimated using all three techniques. The state of the art nanobeam electron diffraction using STEM also provides a strain sensitivity in the order of 10^{-4} . We note that the residual strain maps derived from confocal Raman imaging [see Figs. 4(e) and 4(f)] provide a reliable and non-destructive,

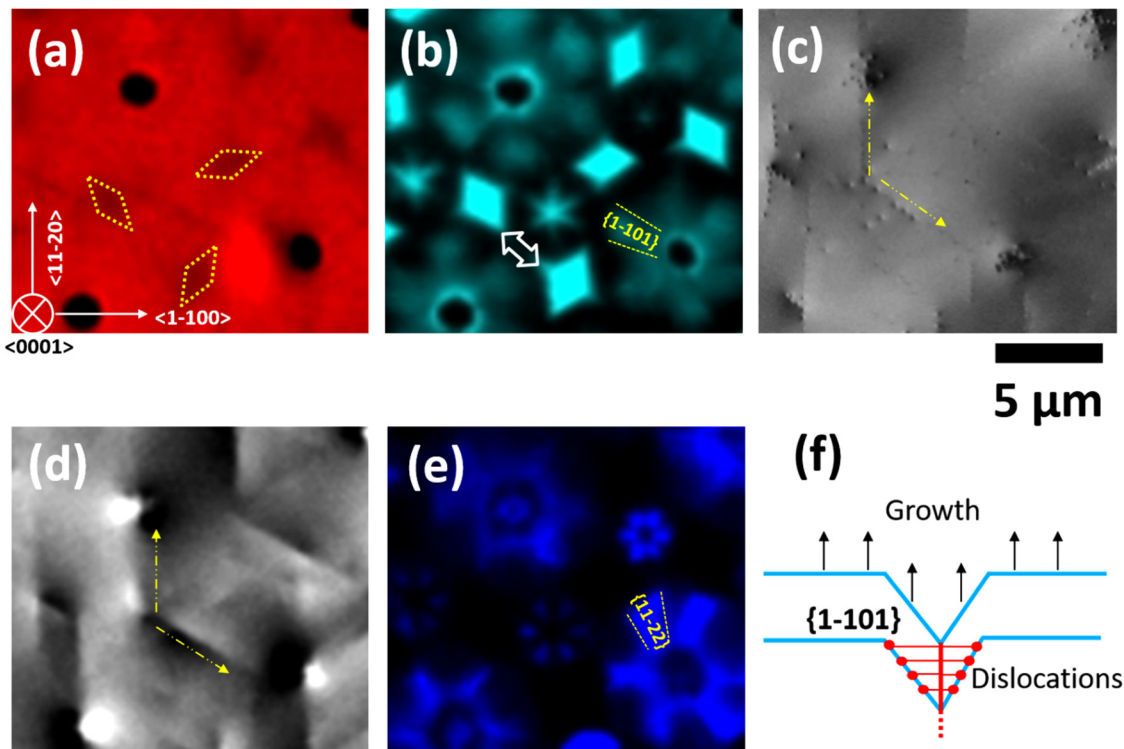


FIG. 5. Correlative confocal Raman and ECCI micrographs. (a) Raman E_2 intensity image showing the location of the nanodashes highlighted by dotted yellow dashes, (b) Raman A_1 peak intensity image revealing the location of the first coalescence marked using a double-sided white arrow, (c) ECCI revealing the position of dislocations and the yellow arrow points the dislocation line-up (d) E_2 peak position showing dislocation line-up direction and merging location at the center of the inverted pyramid, (e) A_1 peak position image showing the semipolar planes and the location of the inverted pyramid, and (f) schematic explaining the dislocation line-up mechanism.

rapid, and statistically significant method of residual strain analysis for the 3D growth of semiconductors. Doping will affect the strain sensitivity of CL and Raman spectroscopy. High doping density may induce EBSD pattern degradation, which affects strain sensitivity.

D. Dislocation distribution and nanodash GaN growth modes

We also use the information gained from correlative microscopy to understand the nanodash GaN growth modes. Figures 5(a)–5(e) show the confocal Raman and ECCI micrographs from the same area revealing the positions of TDs with respect to the nanodashes. From the ECCI micrograph, three main features within the dislocation distributions can be seen: (i) clustering of dislocations in a periodic pattern with circular clusters; (ii) the arrangement of groups of dislocations along distinct lines, angled at 60° intervals; and (iii) occasional individual dislocations. The ECCI micrograph shown in Figs. 3(a) and 5(c) show circular clusters arranged in a hexagonal pattern with an average spacing of $\approx 11\ \mu\text{m}$. This area corresponds to the nanodash pattern of a large inverted pyramid [see Figs. 5(b) and 5(e)]. Comparing Figs. 5(c) and 5(d) comprising the ECCI micrograph and the Raman E_2 peak position image show alignment between the dislocations aligned along $\langle 11-20 \rangle$ and the edge of $\{1-101\}$ facets forming the inverted pyramid. Comparing the location of the nanodashes and the position of dislocations, only a tiny proportion of the total number of dislocations coincide with the growth window, verifying that efficient cancellation or bending of dislocations occurs in the initial stages of growth. It can be seen that some regions covering the first coalescence of the dashes [see the double headed arrow in Fig. 5(b)] are defect free, implying that either the dislocations generated at the coalescence boundaries are mobile as the growth proceeds, or none are created. The organization of dislocations in clusters and lines, with an identified pattern, was discussed in Ref. 14. As shown schematically in Fig. 5(f), dislocations existing on the $\{1-101\}$ facets may bend and propagate parallel to the $\langle 0001 \rangle$ direction along preferential directions (in this case mainly in the $\langle 1-100 \rangle$ directions). They may then bend again and propagate in the $\langle 0001 \rangle$ direction emerging at the center of the inverted pyramid [see Figs. 5(b) and 5(e)], or they may bend again and propagate in the $\langle 0001 \rangle$ direction, or in a direction at an angle to the surface normal leading to the formation of the inclined dislocations, when they meet the intersections of $\{1-101\}$ facets, leading them to align along the $\langle 11-20 \rangle$ directions as observed in Figs. 5(c) and 5(d). An alternative explanation is that lines of defects along the $\langle 11-20 \rangle$ directions could have been created by the coalescence between opposite $\{1-101\}$ planes. The nanodash density was found to substantially impact the dislocation density,¹⁴ with a lower dash density resulting in lower dislocation density due to a reduced number of coalescence points. Comparing the confocal Raman and ECCI micrographs reveals that in the first coalescence stage where the nanodashes meet with each other, few dislocations may be formed at the coalescence boundary. As the growth proceeds, some of the dislocations become mobile and during the second coalescence stage, when opposite $\{1-101\}$ planes merge, new dislocations are formed. A plausible explanation after this stage is that some of the newly formed dislocations may move and

become pinned at a common point where they could not move further as there are no more coalescence fronts beyond this stage of the growth. Therefore reducing the number of coalescence points could be key in reducing the dislocation density.

IV. CONCLUSIONS

In summary, we have demonstrated an alternative approach to understanding the 3D growth of a nanodash GaN thin film and simultaneously studied its physical properties. Residual strain maps produced from the same area by means of three different techniques—namely, EBSD, CL, and confocal Raman imaging—reveal comparable magnitude and direction of the strain. The strain analysis methods are non-destructive and provide high sensitivity for strain measurements of the order of 10^{-4} . We also demonstrated the advantage of confocal imaging where different stages of the crystal growth were evaluated without interrupting the growth, thereby aiding understanding of the different growth stages. The non-destructive approach presented in this work can be adopted for any thin film growth, especially heteroepitaxial growth using selective masks on those substrates where the morphology influences the subsequent growth.

SUPPLEMENTARY MATERIAL

See the [supplementary material](#) for a large area optical microscope image, confocal Raman image, and time-lapse video showing the evolution of the nanodash, ECCI micrographs acquired under different diffraction conditions to identify dislocation types, representative CL spectra, and normal and shear strain maps from HR-EBSD.

ACKNOWLEDGMENTS

This work was supported by the EPSRC projects “Quantitative non-destructive nanoscale characterization of advanced materials” (No. EP/P015719/1), “Manufacturing of nano-engineered III-N semiconductors” (No. EP/M022862/1), and “Nanoscale characterization of nitride semiconductor thin films using EBSD, ECCI, CL, and EBIC” (Nos. EP/J015792/1 and EP/J016098/1).

AUTHOR DECLARATIONS

Conflict of Interest

The authors have no conflicts to disclose.

DATA AVAILABILITY

The data that support the findings of this study are openly available in University of Strathclyde research portal at <https://doi.org/10.15129/659ff01d-e5e0-4868-aaf2-1f3d656f5db3> (Ref. 31). Alternatively, they are also available from the corresponding author upon reasonable request.

REFERENCES

- ¹D. Cooper, T. Denneulin, N. Bernier, A. Beche, and J.-L. Rouviere, *Micron* **80**, 145 (2016).
- ²S. L. Brantley, J. D. Kubicki, and F. White, *Kinetics of Water-Rock Interaction* (Springer-Verlag, New York, 2008).

- ³F. C. Frank, "The influence of dislocations on crystal growth," *Discuss. Faraday Soc.* **5**, 48 (1949).
- ⁴M.-Y. Xie, F. Tasnadi, I. A. Abrikosov, L. Hultman, and V. Darakchieva, *Phys. Rev. B* **86**, 155310 (2012).
- ⁵Y. Taniyasu, M. Kasu, and T. Makimoto, *Nature* **441**, 325 (2006).
- ⁶J. Miao, P. Charalambous, J. Kirz, and D. Sayre, *Nature* **400**, 342 (1999).
- ⁷R. A. Schwarzer, D. P. Field, B. L. Adams, M. Kumar, and A. J. Schwartz, *Electron Backscatter Diffraction in Materials Science* (Springer, New York, 2009).
- ⁸H. Kriaa, A. Guitton, and N. Maloufi, *Sci. Rep.* **7**, 9742 (2017).
- ⁹P. R. Edwards and R. W. Martin, *Semicond. Sci. Technol.* **26**, 064005 (2011).
- ¹⁰S. Nagarajan and M. Sopanen, *J. Phys. D: Appl. Phys.* **49**, 465303 (2016).
- ¹¹Y. Nanishi, *Nat. Photonics* **8**, 884 (2014).
- ¹²A. Vilalta-Clemente, G. Naresh-Kumar, M. Nouf-Alleghiani, P. Gamarra, M. A. Di Forte-Poisson, C. Trager-Cowan, and A. J. Wilkinson, *Acta Mater.* **125**, 125 (2017).
- ¹³A. J. Wilkinson, G. Meaden, and D. J. Dingley, "High-resolution elastic strain measurement from electron backscatter diffraction patterns: New levels of sensitivity," *Ultramicroscopy* **106**, 307 (2006).
- ¹⁴E. D. Le Boulbar, J. Priesol, M. Nouf-Alleghiani, G. Naresh-Kumar, S. Fox, C. Trager-Cowan, A. Satka, D. W. E. Allsopp, and P. A. Shields, *J. Cryst. Growth* **466**, 30 (2017).
- ¹⁵M. Kuball, *Surf. Interface Anal.* **31**, 987 (2001).
- ¹⁶S. McAughtrie, K. Lau, K. Faulds, and D. Graham, *Chem. Sci.* **4**, 3566 (2013).
- ¹⁷T. Batten and O. Milikofu, *Mater. Sci. Forum* **821–823**, 229 (2015).
- ¹⁸Z. Zhang, Z. Xu, Y. Song, T. Liu, B. Dong, J. Liu, and H. Wang, *Nanotechnol. Precis. Eng.* **4**, 023002 (2021).
- ¹⁹L. Reimer, *Scanning Electron Microscopy* (Springer, New York, 1985).
- ²⁰J. I. Goldstein, D. E. Newbury, P. Echlin, D. C. Joy, C. E. Lyman, E. Lifshin, L. Sawyer, and J. R. Michael, *Scanning Electron Microscopy and X-Ray Microanalysis* (Springer, Boston, 2003).
- ²¹J. Christen, M. Grundmann, and D. Bimberg, *J. Vac. Sci. Technol. B* **9**, 2358 (1991).
- ²²G. Naresh-Kumar, J. Bruckbauer, P. R. Edwards, S. Krausel, B. Hourahine, R. W. Martin, M. J. Kappers, M. A. Moram, S. Lovelock, R. A. Oliver, C. J. Humphreys, and C. Trager-Cowan, *Microsc. Microanal.* **20**, 55 (2014).
- ²³A. Winkelmann, G. Nolze, S. Vespucci, N. Gunasekar, C. Trager-Cowan, A. Vilalta-Clemente, A. J. Wilkinson, and M. Vos, *J. Microsc.* **267**, 330 (2017).
- ²⁴G. Naresh-Kumar, B. Hourahine, P. R. Edwards, A. P. Day, A. Winkelmann, A. J. Wilkinson, P. J. Parbrook, G. England, and C. Trager-Cowan, *Phys. Rev. Lett.* **108**, 135503 (2012).
- ²⁵K. J. Lethy, P. R. Edwards, C. Liu, W. N. Wang, and R. W. Martin, *J. Appl. Phys.* **112**, 023507 (2012).
- ²⁶W. Shan, R. J. Hauenstein, A. J. Fischer, J. J. Song, W. G. Perry, M. D. Bremser, R. F. Davis, and B. Goldenberg, *Phys. Rev. B* **54**, 13460 (1996).
- ²⁷V. Yu. Davydov, Yu. E. Kitaev, I. N. Goncharuk, A. N. Smirnov, J. Graul, O. Semchinova, D. Uffmann, M. B. Smirnov, A. P. Mirgorodsky, and R. A. Evarestov, *Phys. Rev. B* **58**, 12899 (1998).
- ²⁸V. Yu. Davydov, N. S. Averkiev, I. N. Goncharuk, D. K. Nelson, I. P. Nikitina, A. S. Polkovnikov, A. N. Smirnov, and M. A. Jacobson, *J. Appl. Phys.* **82**, 5097 (1997).
- ²⁹A. J. Wilkinson, G. Meaden, and D. J. Dingley, "High resolution mapping of strains and rotations using electron backscatter diffraction," *Mater. Sci. Technol.* **22**, 1271 (2006).
- ³⁰A. J. Wilkinson, "Measurement of elastic strains and small lattice rotations using electron back scatter diffraction," *Ultramicroscopy* **62**, 237 (1996).
- ³¹G. Naresh-Kumar *et al.* (2022). "Data for: 'Non-destructive imaging of residual strains in GaN and their effect on optical and electrical properties using correlative light -electron microscopy'," University of Strathclyde research portal. <https://doi.org/10.15129/659ff01d-e5e0-4868-aaf2-1f3d656f5db3>